



## N<sub>x</sub>O-C Nanocage-mediated high-efficient hydrogen evolution reaction on IrNi@N<sub>x</sub>O-C electrocatalyst



Shanyong Chen<sup>a,1</sup>, Shiyan Wang<sup>b,1</sup>, Panpan Hao<sup>a</sup>, Muhong Li<sup>a</sup>, Yu Zhang<sup>a</sup>, Jia Guo<sup>a</sup>, Weiping Ding<sup>a</sup>, Min Liu<sup>c,\*</sup>, Jinlan Wang<sup>b,\*</sup>, Xuefeng Guo<sup>a,\*</sup>

<sup>a</sup> Key Lab of Mesoscopic Chemistry MOE, School of Chemistry and Chemical Engineering, Nanjing University, 210023 Nanjing, China

<sup>b</sup> School of Physics, Southeast University, 211189 Nanjing, China

<sup>c</sup> School of Physics and Electronics, Central South University, 410083 Changsha, China

### ARTICLE INFO

#### Keywords:

Electro-catalysis  
Hydrogen evolution reaction  
Nanoreactor  
Energy conversion

### ABSTRACT

Development of high-performance and stable electrocatalysts for hydrogen evolution reaction (HER) is crucial for hydrogen economy. Inspired by hydrogen evolution behavior on hydrogenase enzyme, in which the azadithiolate bridging ligand of active center facilitates fast proton shuttling and catalytic turnover, here we present an efficient approach to enhance both HER kinetics and stability realizing on an IrNi@N<sub>x</sub>O-C catalyst with individual IrNi nanoparticle separately confined in N and O co-doped carbon (N<sub>x</sub>O-C) nanocage. Experimental and theoretical investigations indicate that the N<sub>x</sub>O-C nanocage provides proton-adsorbing functionality on raising H<sup>+</sup> coverage over IrNi active centers, resulting in much accelerated HER kinetics. The IrNi@N<sub>x</sub>O-C presents superior HER performances compared to all reported Ir-based catalysts, with overpotential of 22 mV at 100 mA cm<sup>-2</sup>, ultrahigh mass activity of 9.82 A mg<sub>Ir</sub><sup>-1</sup> (-0.050 V vs. RHE) and outstanding durability of 200 h at large current density. This work affords fresh insights/strategies for design of high-performance electrocatalysts

### 1. Introduction

Electrocatalytic water splitting is a clean and effective approach to produce high-purity hydrogen towards the renewable-energy systems [1–4]. To improve cost efficiency, great efforts [5–11] have been devoted to searching for optimal catalysts towards hydrogen evolution reaction (HER). Usually, the platinum (Pt)-based [12–16] and iridium (Ir)-based materials [17–21], showing low overpotential and high current density for HER, have been regarded as the state-of-the-art HER electrocatalysts in acid electrolyte because of their near-zero H<sup>+</sup> adsorption Gibbs free energy ( $\Delta G_{H^+}$ ) [19,22]. However, due to the high cost and scarcity of precious metal, it is of paramount significance to enhance the HER mass activity and then reduce the used dosages of Pt and Ir. Besides, the Pt-based and Ir-based materials are also subjected to activity degradation because of their dissolution and agglomeration during the continuous HER operation in acidic electrolyte [19,23]. Comparatively, the Ir-based materials have attracted special attentions due to relatively more durable operation for HER [19–21].

Design of special nanostructure and optimization of the intrinsic

active sites are two general strategies to improve electrocatalytic performances [24–28]. For instance, Wang et al. reported the RhIr nanosheets on three-dimension (3D) Ni foam [29] and Fe/Rh codoped Ni<sub>2</sub>P nanosheets on 3D Ni foam [30] as effective HER catalysts due to the ultrathin nanosheet structure exposing abundant active sites and facilitating the electron/mass transfer. Furthermore, the intrinsic HER activity of precious-metal-based catalysts could be improved through engineering the geometry and electronic structure, such as the alloying strategy [31,32], regulating the strain [33,34] and atom coordination environments [35–38], and modulating hydrogen adsorption/desorption [17], due to the optimized  $\Delta G_{H^+}$  on metal surface. For instance, Huang et al. [18] reported that the IrNi alloy catalyst showed better HER activity relative to single Ir catalyst. However, the HER behaviour is governed by both the intrinsic activity and reaction kinetics [39]. As mentioned above, great efforts have been devoted to searching for catalysts with high intrinsic activity while limited attentions focus on improving the HER kinetics.

Interestingly, experimental and theoretical studies [40–42] have discovered that HER is sensitive to the concentration of hydrogen

\* Corresponding authors.

E-mail addresses: [minliu@csu.edu.cn](mailto:minliu@csu.edu.cn) (M. Liu), [jlwang@seu.edu.cn](mailto:jlwang@seu.edu.cn) (J. Wang), [guoxf@nju.edu.cn](mailto:guoxf@nju.edu.cn) (X. Guo).

<sup>1</sup> These authors contributed equally.

proton, *i.e.* HER performance is pH dependent, and the higher hydrogen proton concentration (low pH) is usually associated with the faster reaction kinetics and then the better catalytic property. In contrast, the low pH condition will damage the active metal centers, leading to poor stability. To address these issues, the natural [FeFe] hydrogenase enzyme with extremely high efficiency for hydrogen production in relatively high pH conditions has attracted special attention [43–48]. As shown in Fig. 1a, the organic azadithiolate ligands coordinating with active sites in the [FeFe] hydrogenase, functioning as proton relays, could facilitate the H<sub>2</sub> generation [44–46]. According to the theoretical study [48], the ligand confinement environment in hydrogenase plays essential role in tuning energy profiles of HER pathway and reaction kinetics. Recently, a few studies [49,50] reported that some organic ligands directly decorating on the precious metal surface could improve the HER activities, which can be considered similar to proton relays. However, both the hydrogenase enzyme and the organic ligands adsorbed on the precious metal active sites were unstable under the electrocatalytic conditions [47,51], especially for the electrocatalytic HER process because of replacing organic ligands by the generated M-H [51], which might limit the HER performances and the working stability. Inspired by the hydrogen evolution behaviour on hydrogenase enzyme, design of inorganic solid proton-enriching microstructure enclosing the metal active center, to mimic the proton adsorption and transfer function as the organic ligands in hydrogenase enzyme, is highly desirable to accelerate the HER kinetics and prevent the agglomeration

of metal nanoparticles to achieve outstanding stability simultaneously. Therefore, different from the general optimized strategy by engineering intrinsic active sites, there is another feasible approach to break through the limitation of the improvement of HER performances with incorporation of inorganic solid proton adsorption-sites surrounded active centers. However, it has been far less investigated to date.

According to our previous study [52], nitrogen and oxygen groups on the N,O co-doped carbon matrix (N,O-C) contributed to the pseudocapacitance through the faradaic redox reaction in acid media, *i.e.* reversible proton coupled electron transfer reaction. This means that the N,O groups could readily adsorb protons from bulk electrolyte into inner Helmholtz plane (IHP) and then reversibly react with them. Therefore, the N,O-C may be used as the inorganic solid surrounded microstructure for proton enrichment and enhanced reaction kinetics (Fig. 1b), similar to the proton relay function of organic ligands in hydrogenase. Inspired by these, we have performed preliminary theoretical calculation. As shown in Fig. 1c-d, the distance (*d*) between the water molecule and the substrate is 1.82 and 2.27 Å for the N,O-C and pure carbon matrix, respectively. The decreased *d* value after introduction of N/O dopants indicates that hydronium ion is more prone to access N,O-C surface, that is, the N/O co-doping may facilitate the proton enrichment. As a proof-of-concept example, we fabricate a unique nanoreactor catalyst in which the individual IrNi nanoparticle is confined in single N/O co-doped carbon nanocage (IrNi@N,O-C) through using a flower-like Ni(OH)<sub>2</sub> nanosheet as reactive template and quinone-amine polymer as the

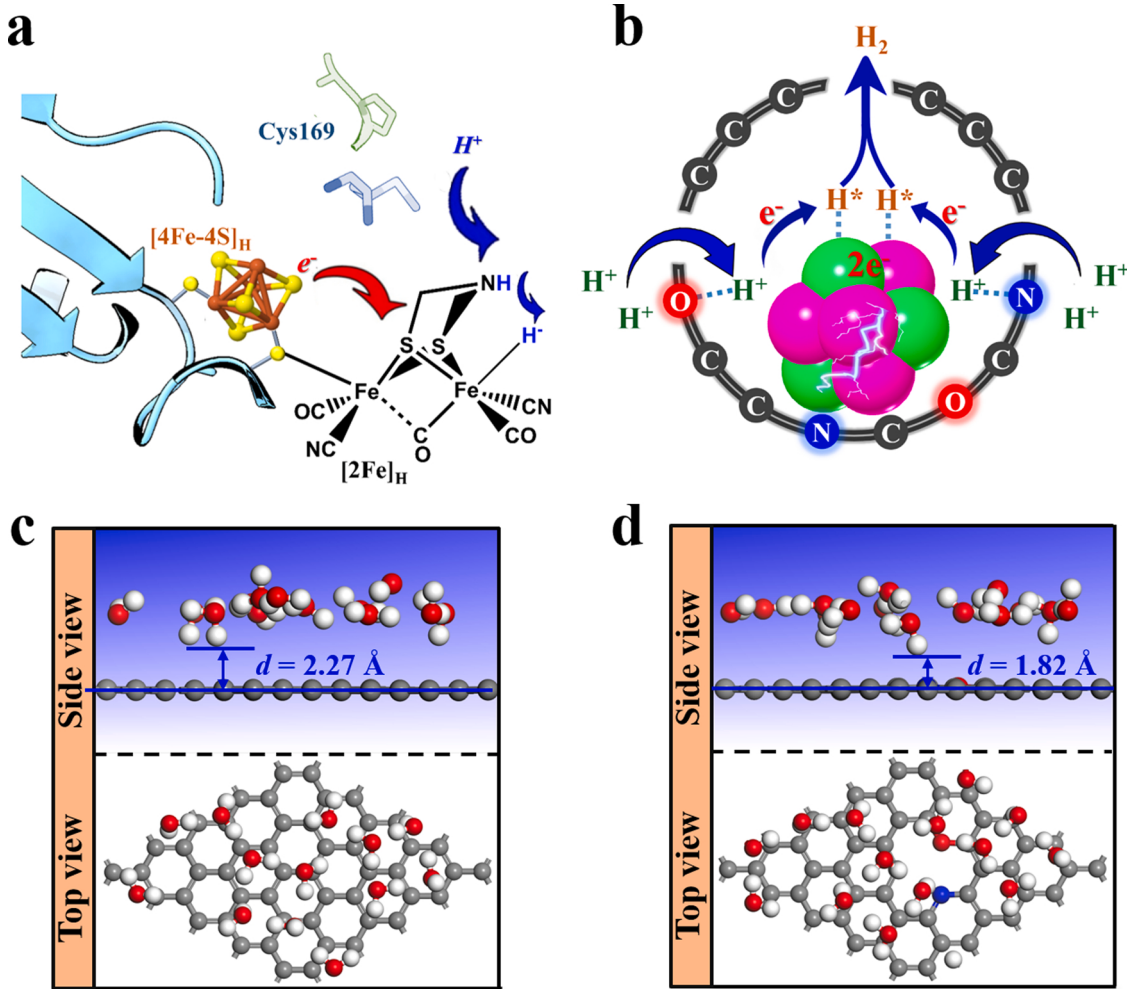


**Fig. 1.** The mechanism for HER. a, Schematic diagram of hydrogen evolution behavior on [FeFe] hydrogenase enzyme. b, Design of proton-enriching microstructure in IrNi@N,O-C for enhanced HER kinetics. c, d, Top and side views of the optimized structure of 13 H<sub>2</sub>O molecule on graphene (c) and N,O-C (d). *d* is the distance between water molecule and substrate.

carbon precursor. The prepared IrNi@N<sub>x</sub>O-C shows superior HER performance in 1 M HClO<sub>4</sub> with the low overpotentials of 22 mV at 100 mA m<sup>-2</sup> and of 267 mV at 1000 mA cm<sup>-2</sup>, ultrahigh mass activity of 9.82 A mg<sub>Ir</sub><sup>-1</sup> at -0.050 V (vs. RHE), as well as excellent stability. This activity outperforms those of all reported Ir-based electrocatalysts, to the best of our knowledge. Further studies confirm that through the N and O dopants the local proton concentration around IrNi nanoparticles could be enriched, leading to the accelerated reaction kinetics and outstanding HER performances.

## 2. Experimental section

### 2.1. Chemicals

Nickel acetate tetrahydrate (Ni(CH<sub>3</sub>COO)<sub>2</sub>•4H<sub>2</sub>O) was purchased from Shanghai Chemical Reagent Co. Ltd. Hexamethylenetetramine (C<sub>6</sub>H<sub>12</sub>N<sub>4</sub>) was purchased from Sinopharm Chemical Reagents Co. Ltd. O-phenylenediamine (C<sub>6</sub>H<sub>8</sub>N<sub>2</sub>), p-benzoquinone (C<sub>6</sub>H<sub>4</sub>O<sub>2</sub>), ammonium chloroiride ((NH<sub>4</sub>)<sub>2</sub>IrCl<sub>6</sub>), chloroplatinic acid (H<sub>2</sub>PtCl<sub>6</sub>.6H<sub>2</sub>O) and ruthenium chloride hydrate (RuCl<sub>3</sub>•xH<sub>2</sub>O, 35.0–42.0% Ru basis) were obtained from Shanghai Aladdin Bio-Chem Technology Co., Ltd. Pt/C 20 wt% benchmark catalyst and Nafion solution (5 wt%) were supplied by Alfa Aesar China. All reagents were of analytical grade and directly used without further purification.

### 2.2. Synthesis of Ni(OH)<sub>2</sub> nanosheet template

Typically, 2.48 g of nickel acetate tetrahydrate and 4.21 g of hexamethylenetetramine were dissolved in 30 mL of distilled water to produce a clear solution with vigorous stirring for 30 min. Then this solution was transferred into a 50 mL Teflon-lined stainless steel autoclave and underwent heated treatment at 120 °C for 12 h. Lastly, the collected Ni(OH)<sub>2</sub> was washed by water and ethanol several times and dried at 80 °C electric oven.

### 2.3. Synthesis of IrNi@N<sub>x</sub>O-C

Typically, 0.5 g of obtained Ni(OH)<sub>2</sub> nanosheets were dispersed into 10 mL of distilled water to obtain a homogeneous suspension after vigorous stirring for 10 min. Then the 4 mL of (NH<sub>4</sub>)<sub>2</sub>IrCl<sub>6</sub> solution (Ir content: 3.54 g/L) was added to above Ni(OH)<sub>2</sub> suspension with vigorous stirring for 60 min and then dried by rotary evaporation at 60 °C, resulting in Ir/Ni(OH)<sub>2</sub> mixture. Meanwhile, the quinone-amine polymer precursor was prepared as following. 0.054 g of o-phenylenediamine and 0.16 g of p-benzoquinone were dissolved in 2 mL and 7 mL anhydrous ethanol, respectively. Then the o-phenylenediamine solution was slowly dropped into the p-benzoquinone solution and the dark brown solutions could be obtained. Next, the quinone-amine polymer precursor was dipped into the Ir/Ni(OH)<sub>2</sub> mixture with the incipient impregnation method to an incipient wetted condition and then the quinone-amine polymer coatings formed on the Ir/Ni(OH)<sub>2</sub> surface (denoted as Ir/Ni(OH)<sub>2</sub> @PAQ) after aging for 24 h at room temperature and at 50 °C, respectively. The Ir/Ni(OH)<sub>2</sub> @PAQ mixture was calcined at 300 °C for 2 h and then 650 °C for 2 h at a heating rate of 3 °C/min under Ar protection. The obtained powders were soaked in 0.5 M H<sub>2</sub>SO<sub>4</sub> at 80 °C for 10 h to remove the extra Ni nanoparticles. Lastly, after washing by ethanol and water several times, the final product was dried at an oven of 80 °C for 12 h, denoted as IrNi@N<sub>x</sub>O-C. The IrNi@N<sub>x</sub>O-C<sub>700</sub>, IrNi@N<sub>x</sub>O-C<sub>750</sub>, and IrNi@N<sub>x</sub>O-C<sub>800</sub> were prepared by the same procedures except the temperature of the second heat treatment was adjusted to 700 °C, 750 °C, and 800 °C, respectively. The IrNi/C with the IrNi nanoparticles supported on commercial carbon black (Ketjenblack, EC-600JD) was produced by traditional hydrogen reduction route. The IrNi@N-C and IrNi@O-C were prepared via the same procedure as IrNi@N<sub>x</sub>O-C but replacement of quinone-amine polymer with o-phenylenediamine and p-benzoquinone as the carbon

precursor, respectively. The PtNi@N<sub>x</sub>O-C and RuNi@N<sub>x</sub>O-C were prepared through the same procedure as IrNi@N<sub>x</sub>O-C but using H<sub>2</sub>PtCl<sub>6</sub>.6H<sub>2</sub>O and RuCl<sub>3</sub>•xH<sub>2</sub>O as Pt and Ru precursors, respectively. The IrNi@N<sub>x</sub>O-C was subjected to H<sub>2</sub> reduction treatment at 550 °C for 5 h to obtain IrNi@N<sub>x</sub>O-C-H<sub>2</sub>.

### 2.4. Characterizations

Powder X-ray diffraction (XRD) measurements were carried out on a Shimadzu XRD-6000 diffractometer (Cu K $\alpha$  radiation,  $\lambda = 1.54$  Å). The metal loadings were confirmed by inductively coupled plasma atomic emission spectrometry (ICP-AES) on Optima 5300 DV. Scanning electron microscopy (SEM) was conducted on a Hitachi field emission scanning electron microscopy transmission (FESEM, S-4800). Transmission electron microscopy (TEM) and high-angle annular dark-field-TEM (HAADF-TEM) images were acquired from the JEOL JEM-2100 and the FEI Talos F200x both with the same accelerating voltage of 200 kV. The nitrogen adsorption desorption isotherms were performed on the Micromeritics ASAP 2020. The specific surface area was analyzed by the Brunauer–Emmett–Teller (BET) method. Raman spectra were collected from a Renishaw inVia spectrometer. X-ray photoelectron spectroscopy (XPS) measurements were conducted on a PHI 5000 Versa Probe with Al K $\alpha$  radiation and the binding energies were calibrated referring to the C 1 s peak of 284.6 eV. X-ray absorption near-edge spectroscopy (XANES) experiments were operated on the beamline BL12B-a in National Synchrotron Radiation Laboratory (NSRL). FT-IR spectra were recorded on the Thermo fisher Nicolet iS10 instrument. Contact angle experiments were conducted on Kruss K100.

### 2.5. Electrochemical measurements

The HER performance evaluation was conducted on a CHI760D Electrochemical Workstation using a three-electrode system. The saturated calomel electrode (SCE) was used as the reference electrode in acid electrolytes (1 M HClO<sub>4</sub> and 0.1 M HClO<sub>4</sub>) and a Hg/HgO reference electrode was used in alkaline electrolytes (1 M KOH and 0.1 M KOH). The counter electrode is a graphite rod for all measurements. The typical working electrode of IrNi@N<sub>x</sub>O-C was prepared as following. Firstly, 3 mg of the catalysts and 20  $\mu$ L of Nafion (5 wt%) were added into 0.980 mL of isopropanol and then were dispersed by sonication for 1 h to form a homogeneous ink. Lastly, 4  $\mu$ L of the ink was loaded on the polished glassy carbon electrode (GCE, area: 0.07065 cm<sup>2</sup>) and dried at room temperature (catalyst loading: 0.17 mg cm<sup>-2</sup>, Ir loading: 0.026 mg<sub>Ir</sub> cm<sup>-2</sup>). For comparison, the commercial Pt/C catalyst (20 wt %) electrode also was prepared with the loading of 0.14 mg cm<sup>-2</sup> (Pt loading: 0.028 mg<sub>Pt</sub> cm<sup>-2</sup>). Before collecting the linear sweep voltammograms (LSV) curve, the working electrodes were first activated by scanning CV curves for 50 cycles with the potential ranges from 0.05 to 1.05 V (vs. RHE) at a scan rate of 100 mV s<sup>-1</sup> until stable currents were acquired in N<sub>2</sub> purged electrolyte. After the activation process, the LSV curves were collected in a steady state. The LSV were performed in the N<sub>2</sub> purged electrolyte at the sweep rate of 5 mV s<sup>-1</sup>. All the polarization curves were corrected by 85% resistance compensation and were referred to the reversible hydrogen electrode (RHE). The CV stability test was conducted in the potential ranges of +0.5 V to -0.1 V (vs. RHE) with a scan rate of 100 mV s<sup>-1</sup>. The current time curves were collected from the chronoamperometry measurement at the current density of 10 mA cm<sup>-2</sup>. The chronopotentiometry measurement was performed at current density of 500 and 1000 mA cm<sup>-2</sup> for 100 h, respectively. Electrochemical impedance spectroscopy (EIS) data were recorded in the frequency range of 100,000–0.1 Hz at different HER overpotentials. Calibration experiment for SCE reference electrode was carried out in the high-purity H<sub>2</sub>-saturated 1 M HClO<sub>4</sub> using a Pt net as the working electrode and counter electrode. The TOF (s<sup>-1</sup>) was calculated by the formula:

$$\text{TOF} = \frac{I}{2Fn} \quad (1)$$

where  $I$  refers to the corresponding current at the specific HER overpotential,  $F$  represents the Faraday constant,  $n$  is the number of active sites. The  $n$  was calculated by the Cu UPD method. The Faradic efficiency was determined by the equation:

$$\text{Faradic efficiency} = \frac{2F \times N_{H_2}}{It} \quad (2)$$

where  $F$  represents the Faradic constant,  $I$  refers to the current,  $t$  is the running time and  $N_{H_2}$  is the amount of  $H_2$  production. The  $N_{H_2}$  was detected by the gas chromatography.

## 2.6. Computational details

All the first-principles spin-polarized calculations were performed by using plane-wave density functional theory (DFT) as implemented in the Vienna Ab Initio Simulation Package (VASP) [53] with the ion cores represented by the projector augmented wave (PAW) [54] potentials. The electronic exchange-correlation energy was calculated by using Perdew-Burke-Ernzerhof (PBE) function within the generalized gradient approximation (GGA), and the kinetic energy cutoff for the plane-wave basis set was set as 500 eV. The convergence criteria were set to  $10^{-5}$  eV and  $-0.02$  eV/Å for the energy and the forces on each atom, respectively. In order to avoid the interaction between two periodic units, a vacuum space of 15 Å was applied in perpendicular z direction. Grimme's semiempirical DFT-D3 [55] scheme of dispersion correction was considered to describe the weak interactions.

## 3. Results and discussion

### 3.1. Synthesis and characterization of IrNi@N,O-C nanoreactor

As illustrated in Fig. 2a, the IrNi@N,O-C is fabricated via a reactive

template strategy. Firstly, the flower-like  $\text{Ni(OH)}_2$  nanosheets (Fig. 2b), as the reactive template, are mixed uniformly with iridium precursor under stirring solution (experiment details see Experimental section). Then the obtained  $\text{Ir}/\text{Ni(OH)}_2$  is coated by the quinone-amine polymer layer (PAQ) with incipient impregnation method, resulting in the  $\text{Ir}/\text{Ni(OH)}_2 @\text{PAQ}$  composite (Fig. 2c). Finally, after pyrolysis and acid etching treatment, the  $\text{IrNi@N,O-C}$  with the flower-like 3D nanostructure (Fig. 2d) can be obtained. Notably, all the  $\text{Ni(OH)}_2$  precursor, the intermediates and the final product  $\text{IrNi@N,O-C}$  exhibit the similar 3D flower-like morphology (Fig. 2b-d), suggesting that in present reactive template route the  $\text{Ni(OH)}_2$  nanosheets not only serve as the structure template but also provide the nickel precursor to form IrNi alloy (*vide infra*). The morphology characterizations of the final product  $\text{IrNi@N,O-C}$  have been performed by scanning electron microscope (SEM), transmission electron microscopy (TEM) and high-angle annular dark-field-TEM (HAADF-TEM). It can be seen that there are some protuberant spheres embedded on the nanosheet surface of  $\text{IrNi@N,O-C}$  (Fig. 2e). As shown in Figs. 2f and 2h, there is only single nanoparticle of *ca.* 4 nm confined in every carbon cage with diameter about 15 nm. This unique nanostructure can be also verified by the typical HAADF-TEM image of Fig. 2g in which the bright nanoparticles are confined in slightly transparent carbon cages. The HRTEM image (Fig. 2i) shows the lattice fringe of nanoparticle is 0.215 nm, which is slightly smaller than the (111) crystalline plane of face-centered cubic (fcc) Ir (0.222 nm in JCPDS card No.06-0598) but larger than the (111) crystalline plane of fcc Ni (0.203 nm in JCPDS card No.04-0850), indicative of the formation of IrNi alloy nanoparticle [18]. The IrNi alloy is also confirmed by the SAED (inset in Fig. 2i) and XRD measurement (Fig. S1, Supporting Information). Additionally, HAADF-energy-dispersive X-ray spectroscopy (HAADF-EDS) reveals that the bright nanoparticles consist of Ir and Ni and the N and O atoms are uniformly doped in the carbon substrate (Fig. S2, Supporting Information). The  $\text{IrNi@N,O-C}$  nanoreactor with the IrNi nanoparticle confined inside the carbon nanocage has also been confirmed by the TEM tilting technique. As displayed in Fig. S3

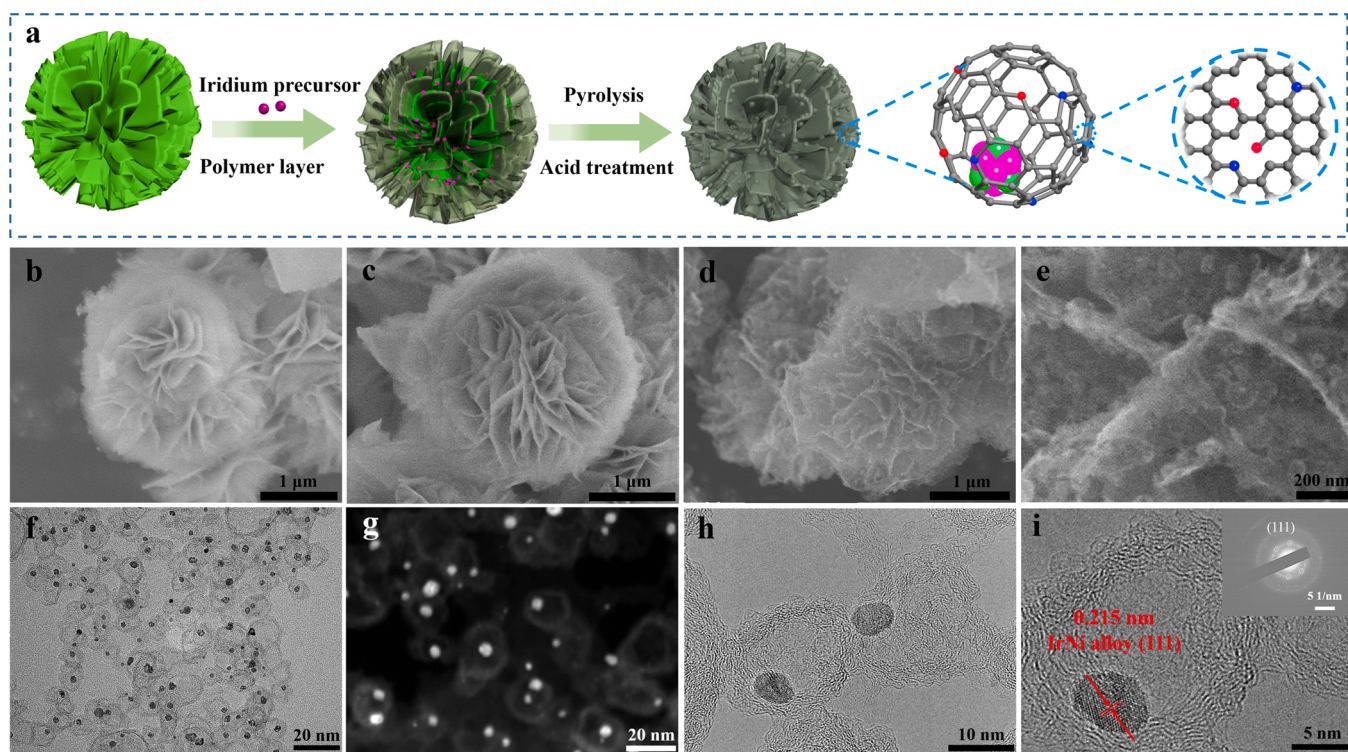


**Fig. 2.** Synthesis and morphology characterization. a, Illustration of the synthesis route of  $\text{IrNi@N,O-C}$ . b, Typical SEM image of the  $\text{Ni(OH)}_2$ . c, Typical SEM image of the  $\text{Ir}/\text{Ni(OH)}_2 @\text{PAQ}$ . d, e, Typical SEM images of  $\text{IrNi@N,O-C}$ . f, Typical TEM, g, HAADF-TEM, and h, HRTEM images of  $\text{IrNi@N,O-C}$ . i, The enlarged HRTEM image and (inset) the corresponding SAED patterns of  $\text{IrNi@N,O-C}$ .

(Supporting Information), the IrNi nanoparticle is indeed included in the nanocage in the X-axis range of  $+20^\circ$  to  $-15^\circ$ .

To understand the formation mechanism of the unique IrNi@N,O-C nanoreactor, the two-step consecutive pyrolysis process (experiment details see Experimental section) has been separately studied. After the initial Ir/Ni(OH)<sub>2</sub> @PAQ composite is heated at 300 °C in Ar flow for 2 h, the obtained Ir/Ni(OH)<sub>2</sub> @PAQ-300 shows nickel nanoparticles with the particle diameter of 5–15 nm (Fig. S4 and S5, Supporting Information). When the initial Ir/Ni(OH)<sub>2</sub> @PAQ undergo the whole heat treatment with 300 °C for 2 h and 650 °C for 2 h, the obtained Ni/IrNi@N,O-C shows an amount of aggregated large Ni nanoparticles out of the distinct IrNi@N,O-C nanoreactor nanostructure (Fig. S6, Supporting Information). Notably, the diameters of Ni nanoparticles forming at 300 °C are equivalent to those of carbon nanocages in the final IrNi@N,O-C, suggesting the initial Ni nanoparticles catalyze the carbon precursors to generate the carbon nanocages [56], and after that, a part of nickels migrate out of the nanocages to form large Ni nanoparticles at high-temperature conditions due to its relatively low melting point, resulting in the coexistence of large Ni nanoparticles and IrNi@N,O-C nanoreactor for Ni/IrNi@N,O-C. After removing the large Ni nanoparticles by acid etching from Ni/IrNi@N,O-C, the final IrNi@N,O-C nanoreactor nanostructure can be obtained (Illustration of the formation mechanism see Fig. S7, Supporting Information).

Fig. 3a shows that the N<sub>2</sub> adsorption and desorption isotherms of IrNi@N,O-C are type IV with a hysteresis loop ( $p/p_0$  at 0.4–0.6), indicative of the existence of mesopores. Additionally, the isotherms have a sharp knee at low relative pressure, suggesting the presence of a narrow micropore size distribution. As displayed in Fig. 3b, the IrNi@N,O-C shows apparent micropores with the size of  $\sim 1.3$  nm and multiple mesopores. The micropores may be assigned to the pores existed in the carbon cage shell, while the mesopores with size of 10–20 nm could be attributed to the carbon cages, consistent with the TEM results. Brunauer-Emmett-Teller (BET) surface area of IrNi@N,O-C is calculated to be 441 m<sup>2</sup>/g with the pore volume of 1.15 cm<sup>3</sup>/g. These results from N<sub>2</sub> sorption analysis further confirm the unique structure of IrNi@N,O-C nanoreactor.

X-ray absorption near-edge spectroscopy (XANES) and X-ray photoelectron spectroscopy (XPS) have been used to study chemical configuration and electronic state of IrNi@N,O-C (Fig. 3c-f). The C K-edge XANES spectrum (Fig. 3c) shows three peaks (C1: 284.4 eV, C2: 287.5 eV, and C3: 291.3 eV), in which the C1 and C3 are attributed to the  $\pi^*_{\text{C-C}}$  and  $\sigma^*_{\text{C-C}}$  structure [57], respectively. The distinct C2 peak is related to  $\pi^*_{\text{C-O/N-C}}$  structure [57], indicating the successful doping of N and O in C framework. According to the XPS measurement, the contents of N and O reach up to 6.8 at% and 8.0 at%, respectively. The high contents of N and O dopants could be also verified by the relatively high value of  $I_D/I_G$  in Raman measurement (Fig. S8, Supporting Information). The N1s XPS shows four kinds of N species, including pyridinic-N (N1, 398.4 eV, 2.05 at%), pyrrolic-N (N2, 399.6 eV, 0.77 at%), graphitic-N (N3, 400.8 eV, 3.26 at%), and oxidized-N (N4, 403.6 eV, 0.72 at%) [58]. And the deconvolution of O 1s XPS spectrum determines the three kinds of O species, including O1 group (i.e., O<sup>2-</sup>=C, 531.4 eV, 4.08 at%), O2 group (i.e., C-O<sup>2-</sup>-H phenol and/or C-O<sup>2-</sup>-C ether, 533.2 eV, 3.06 at%), O3 group (i.e., chemisorbed oxygen, 535.3 eV, 0.86 at%) [59–61]. Meanwhile the N and O dopants display explicit characteristic peaks in N K-edge and O K-edge XANES (Fig. S9, Supporting Information), consistent with the XPS results. Interestingly, the splitting N1' peak in N K-edge XANES and the emerging O3 peak in O K-edge XANES indicate the existence of interaction between the IrNi nanoparticles and the adjacent N and O groups. To elucidate the interaction, the IrNi alloys supported on commercial carbon (IrNi/C) have been prepared through the traditional impregnation and H<sub>2</sub> reduction route (The related details see Fig. S10 and S11, Supporting Information). Based on the XPS results, for both of the IrNi@N,O-C and the IrNi/C, the iridium exists mainly in the form of metallic state (Fig. 3d and Fig. S12a, Supporting Information) and the nickel shows coexistence of oxidized state and metallic state (Fig. S12b and S13, Supporting Information), probably due to the exposure at aerobic atmosphere [62]. And according to the ICP-AES measurement for IrNi@N,O-C, the Ir and Ni contents are determined to be 15.3 wt% and 3.8 wt% (Atomic ratio of Ir to Ni is 1.23:1), respectively. It should be pointed out that both of the Ir 4f (4f<sub>7/2</sub> and 4f<sub>5/2</sub>) and Ni 2p (2p<sub>3/2</sub> and 2p<sub>1/2</sub>) peaks for IrNi@N,O-C shift to a

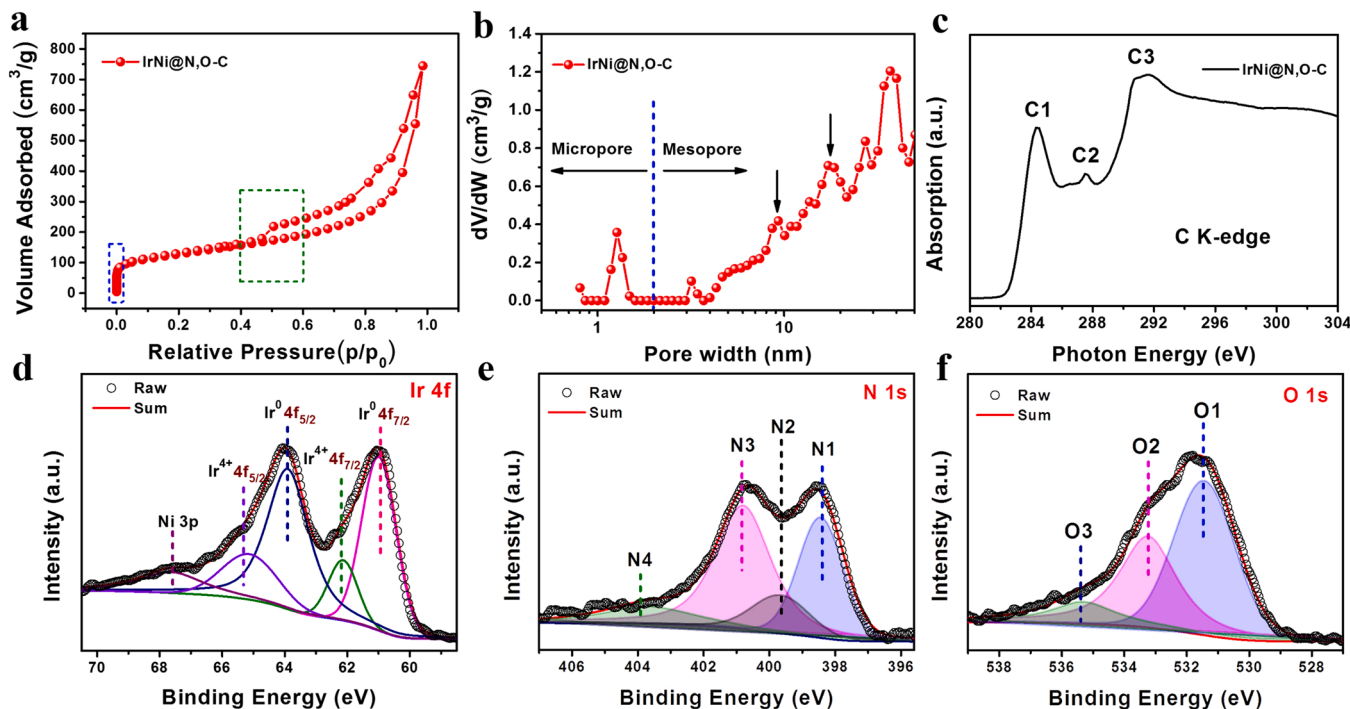


Fig. 3. Nanostructure and spectroscopy characterization. a, N<sub>2</sub> adsorption and desorption isotherms of IrNi@N,O-C. b, Pore size distribution of IrNi@N,O-C. c, C K-edge XANES spectrum of IrNi@N,O-C. d, Ir 4f, e, N 1s, and f, O 1s XPS spectra of IrNi@N,O-C.

position with lower binding energy as compared to IrNi/C (Fig. S14, Supporting Information), suggesting the electron transfer from the carbon matrix to the IrNi nanoparticles [63]. This electron interaction enables the IrNi nanoparticles with enriched electron density, which may favor for the electrocatalytic HER process [64].

### 3.2. Electrochemical performance

The HER performances have been evaluated by linear sweep voltammogram (LSV) measurement with scan rate of  $5 \text{ mV s}^{-1}$  at a typical three-electrode setup. Prior to the tests, the reference electrode has been calibrated (Fig. S15, Supporting Information). A series of IrNi@N,O-C samples with different pyrolysis temperature have been prepared (Fig. S16 and S17, Supporting Information) and their catalytic performances are illustrated in Fig. S18 (Supporting Information). Among these samples, the IrNi@N,O-C with pyrolysis temperature of  $650^\circ\text{C}$  shows the best HER activity both in  $1 \text{ M HClO}_4$  and  $0.1 \text{ M HClO}_4$  and thus it has been chosen as the representative to further investigate the HER performances. To exclude the mass-transfer influence, we have compared the HER performances of IrNi@N,O-C on glassy carbon and on rotating disk electrode (Fig. S19, Supporting Information).

Fig. 4a shows the polarization curves with iR correction of IrNi@N,O-C, commercial Pt/C, and IrNi/C (Raw polarization curves see Fig. S20, Supporting Information) performed in  $1 \text{ M HClO}_4$ . To achieve the current density of  $10 \text{ mA cm}^{-2}$  ( $\eta_{10}$ ), the overpotential of IrNi@N,O-C only needs  $6 \text{ mV}$ , which is smaller than that of Pt/C ( $16 \text{ mV}$ ) and IrNi/C ( $26 \text{ mV}$ ) and outperforms most of advanced precious metal based electrocatalysts (Table S1, Supporting Information). Note that the HER activity of commercial Pt/C in this work ranks at the top level as compared to the reported results (Table S2, Supporting Information). More impressively, the  $\eta_{100}$  of IrNi@N,O-C is  $22 \text{ mV}$ , much smaller than Pt/C ( $99 \text{ mV}$ ) and IrNi/C ( $120 \text{ mV}$ ), indicative of superior activity of IrNi@N,O-C (Fig. 4b). The slight increase of overpotential (range from  $\eta_{10}$  to  $\eta_{100}$ :  $16 \text{ mV}$ ) leads to the great increment of current density of  $90 \text{ mA cm}^{-2}$  suggesting the fast reaction kinetics, which is very appealing to the practical application. It is noteworthy that the IrNi@N,

O-C exhibits the similar  $\eta_{10}$  to that of the reported most advanced Ir-based HER catalyst (IrHNC) [17] ( $\eta_{10}$  of IrNi@N,O-C:  $6 \text{ mV}$  vs  $\eta_{10}$  of IrHNC:  $4.5 \text{ mV}$ ), but shows much smaller  $\eta_{100}$  than that of IrHNC ( $\eta_{100}$  of IrNi@N,O-C:  $22 \text{ mV}$  vs  $\eta_{100}$  of IrHNC:  $39 \text{ mV}$ ), verifying the enhanced kinetics towards the further improvement of HER performance. The fast reaction kinetics of IrNi@N,O-C is also confirmed by the small Tafel slope ( $18 \text{ mV dec}^{-1}$ ) in Fig. 4c. As we all known, a typical Tafel process in acid media, i.e.  $\text{H}^* + \text{H}^* \rightarrow \text{H}_2$ , is related to the Tafel slope of  $\text{ca. } 30 \text{ mV dec}^{-1}$ . Herein, the IrNi@N,O-C exhibits the Tafel slope of  $18 \text{ mV dec}^{-1}$ , less than that of Pt/C ( $28 \text{ mV dec}^{-1}$ ), indicating there is an optimized reaction path for IrNi@N,O-C accounting for the enhanced reaction kinetics. Furthermore, according to the Butler–Volmer equation, IrNi@N,O-C displays a high exchange density of  $4.08 \text{ mA cm}^{-2}$  (Fig. S21, Supporting Information), suggesting the high intrinsic activity.

To further study the intrinsic activity, the number of active sites has been measured by Cu underpotential deposition (UPD) method [65]. As shown in Fig. 4d, after introducing  $\text{Cl}^-$ , the Cu UPD and overpotential deposition (OPD) peaks and their corresponding stripping peaks could be separated distinctly. Then a series of LSV curves with varying initial potential from  $0.20 \text{ V}$  to  $0.27 \text{ V}$ , referring to the stripping of deposited Cu, have been collected (Fig. S22, Supporting Information). Through integrating these peaks in LSV data the corresponding charges against different potentials could be obtained (Fig. 4e) and thus the density of active sites for IrNi@N,O-C are calculated to be  $4.21 \times 10^{20}$  sites per gram by the platform charge of  $\text{ca. } 0.16 \text{ mC}$  (Table S3, Supporting Information). The same experiments have also been conducted for Pt/C and IrNi/C (Fig. S23, Supporting Information) and the results are depicted in Table S3 (Supporting Information). Further, the turnover frequency (TOF) of the IrNi@N,O-C is determined to be  $5.33 \text{ H}_2 \text{ s}^{-1}$  at  $-0.025 \text{ V}$  (Fig. 4f), which is  $6.2$  and  $18$  times higher than that of Pt/C and IrNi/C, respectively. Remarkably, the IrNi@N,O-C presents a record high mass activity of  $4.68 \text{ A mg}_{\text{Ir}}^{-1}$  at  $-0.025 \text{ V}$  and  $9.82 \text{ A mg}_{\text{Ir}}^{-1}$  at  $-0.05 \text{ V}$  (Fig. 4f) relative to the reported Ir-based materials (Table S1). Considering activity parameters in whole (Fig. 5a), the HER performances of IrNi@N,O-C exceed all reported Ir-based catalysts,

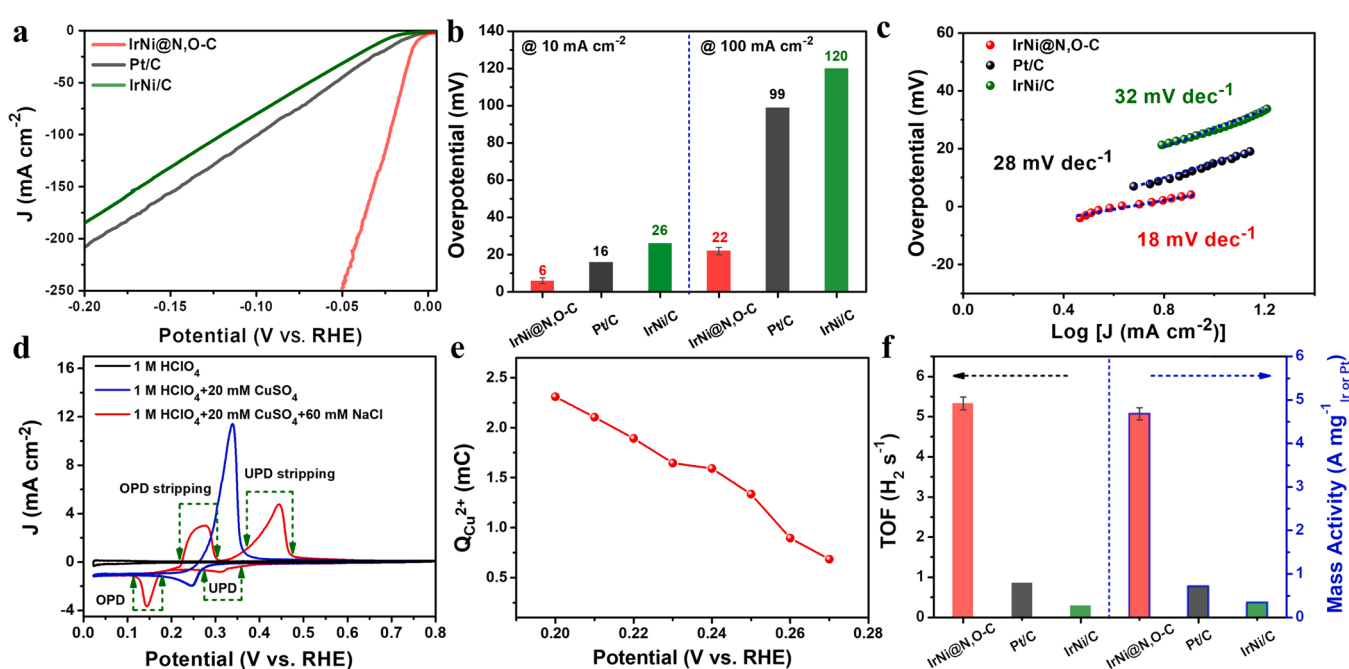
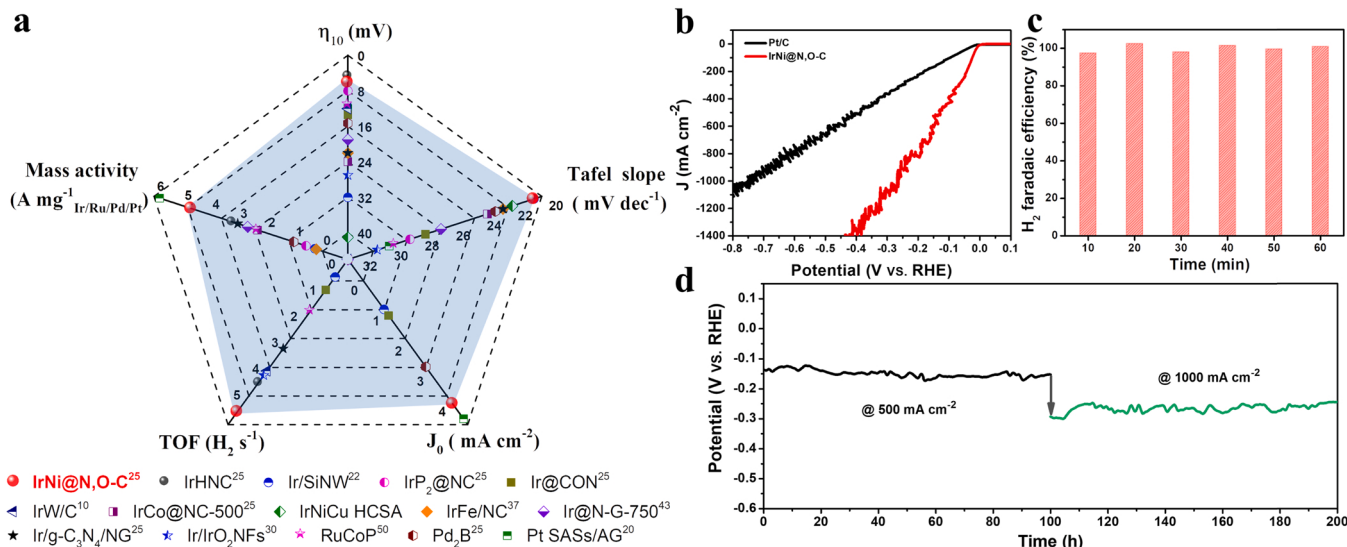


Fig. 4. Electrocatalytic performance of different catalysts. a, HER polarization curves of IrNi@N,O-C, Pt/C, and IrNi/C. b, Overpotential at  $10 \text{ mA cm}^{-2}$  and  $100 \text{ mA cm}^{-2}$  for IrNi@N,O-C, Pt/C, and IrNi/C. c, Tafel slopes of IrNi@N,O-C, Pt/C, and IrNi/C. d, Cyclic voltammometry curves of IrNi@N,O-C in different solutions. e, The calculated charge quantities at varying potentials according to Cu UPD method. f, The TOF and mass activity of IrNi@N,O-C, Pt/C, and IrNi/C at  $-0.025 \text{ V}$  (The data of error bar were collected from three independent measurements).



**Fig. 5.** HER performance and stability. a, Comprehensive comparison of the various activity parameters with reported catalysts. The detailed HER performances and referenced literatures of the representative catalysts can see the blue part in Table S1 (Supporting Information). The superscript numbers on representative catalysts refer to the overpotential (mV) for achieving the corresponding TOF and mass activity and the all values closer to the perimeter indicates better activity. b, HER polarization curves of IrNi@N,O-C and Pt/C with large current density. c, H<sub>2</sub> faradaic efficiency of IrNi@N,O-C at 200 mA cm<sup>-2</sup>. d, Chronopotentiometry (CP) test of IrNi@N,O-C at 500 mA cm<sup>-2</sup> and 1000 mA cm<sup>-2</sup> for 100 h, respectively.

state-of-the-art Ru-based and Pd-based catalysts, and comparable to the most advanced Pt-based materials in acid media, to the best of our knowledge. More impressively, thanks to the fast HER kinetics, the IrNi@N,O-C shows the overpotential of 267 mV to reach the large current density of 1000 mA cm<sup>-2</sup> (Fig. 5b), significantly smaller than that of Pt/C catalyst (744 mV), indicating the promising potential in the practical application. Importantly, IrNi@N,O-C exhibits the faradaic efficiency of *ca.* 100% towards the H<sub>2</sub> production (Fig. 5c). Furthermore, IrNi@N,O-C also exhibits superior HER activity to Pt/C and IrNi/C in 0.1 M HClO<sub>4</sub>, 0.1 M KOH and 1 M KOH (Fig. S24, Supporting Information). The IrNi@N,O-C presents the η<sub>10</sub> of 28 mV and the mass activity of 2.1 A mg<sub>Ir</sub><sup>-1</sup> at  $-0.07$  V in 1 M KOH (Fig. S25, Supporting Information), far exceeding the commercial Pt/C (η<sub>10</sub> of 47 mV and mass activity of 0.74 A mg<sub>Pt</sub><sup>-1</sup>) under same conditions.

The stabilities of the catalysts have been evaluated by CV cycle, chronoamperometry and chronopotentiometry method in 1 M HClO<sub>4</sub>. As displayed in Fig. S26 (Supporting Information), the LSV polarization curves of IrNi@N,O-C before and after 10,000 CV cycles are highly overlapped, while for Pt/C and IrNi/C the polarization curves after 10,000 CV cycles exhibit apparent negative shifts as compared to the initial curves (Fig. S26 and Fig. S27, Supporting Information). The overpotential at 50 mA cm<sup>-2</sup> of IrNi@N,O-C only negatively shifts 4 mV (Fig. S26, Supporting Information), much smaller than that of Pt/C (26 mV) and IrNi/C (24 mV), indicating the excellent durability of IrNi@N,O-C. For chronoamperometry test, the IrNi@N,O-C shows negligible reduction of current density up to 60 h test while the Pt/C and IrNi/C suffer great loss of current density after 24 h test (Fig. S28, Supporting Information). Impressively, the IrNi@N,O-C could work stably up to 100 h at large current density of 500 and 1000 mA cm<sup>-2</sup>, respectively (Fig. 5d). Furthermore, the sample after CV durability test shows the invariant nanostructure as initial IrNi@N,O-C (Fig. S29, Supporting Information), *i.e.* the IrNi nanoparticles confined in the carbon nanocages, verifying the excellent structural and morphological stability of IrNi@N,O-C. It has been reported that the attenuated catalytic activity of commercial Pt/C catalyst during electrocatalytic process is mainly related to the serious agglomeration of Pt nanoparticles through Ostwald ripening process [23,66]. In the case of IrNi@N,O-C nanoreactor, individual IrNi nanoparticle is confined in a single carbon nanocage and will hardly contact with the other shielded

nanostructures and there is strong interaction between the IrNi nanoparticles and carbon nanocages, which could effectively restrain the physical ripening and the electrochemical dissolution of the IrNi nanoparticles, leading to the outstanding stability during electrocatalytic reaction.

### 3.3. Understanding the enhanced HER kinetics on IrNi@N,O-C nanoreactor

Experimentally, the remarkable HER activity of IrNi@N,O-C has been explored. As shown in Fig. S30a (Supporting Information), after addition of strong poisoning reagent of SCN<sup>-</sup>, the apparent activity decay trend of IrNi@N,O-C is similar to that of Pt/C, indicating that the SCN<sup>-</sup>/H<sup>+</sup> in electrolyte can pass through the micropores (TEM and BET results) in carbon nanocage and thus get access to the active IrNi nanoparticle. Fourier transform infrared spectra (FT-IR) (Fig. 6a) show pronounced O-H stretching peak of water [67] for IrNi@N,O-C immersed in 1 M HClO<sub>4</sub> relative to IrNi/C immersed in 1 M HClO<sub>4</sub>, suggesting the strong affinity to electrolyte for IrNi@N,O-C. The contact angle (CA) experiment (Fig. 6b) confirms that the IrNi@N,O-C with doping of N and O atoms shows better hydrophilicity than IrNi/C, favoring for the accessibility of electrolyte to the active center. Interestingly, the IrNi@N,O-C shows distinctly irregular cyclic voltammetry (CV) curves with oxidation peak (O1) and reduction peak (R1) while the IrNi/C displays rectangle CV (Fig. S30b, Supporting Information), suggesting there is existence of reversible redox reactions for IrNi@N,O-C contributing to the faradaic pseudocapacitance. In light of the generally accepted views in the field of capacitance, the typical reversible redox reaction upon N and O groups [68,69] can be described in Fig. 6b (Bottom). This result indicates the N and O functional groups could readily adsorb H<sup>+</sup> from bulk electrolyte into inner Helmholtz plane (IHP) and then reversibly react with it. Besides, it is reported that the confinement effect in nano-scale is also conducive to the proton enrichment [70]. In the case of IrNi@N,O-C nanoreactor structure, the N and O groups adjacent to the IrNi nanoparticles may serve as the H<sup>+</sup> collector, supplying available and sufficient H<sup>+</sup> for the subsequent HER upon IrNi active centers.

After understanding the enriched H<sup>+</sup> essence of N/O co-doped carbon nanocages, the hydrogen adsorption (H<sup>\*</sup>) behavior over active sites

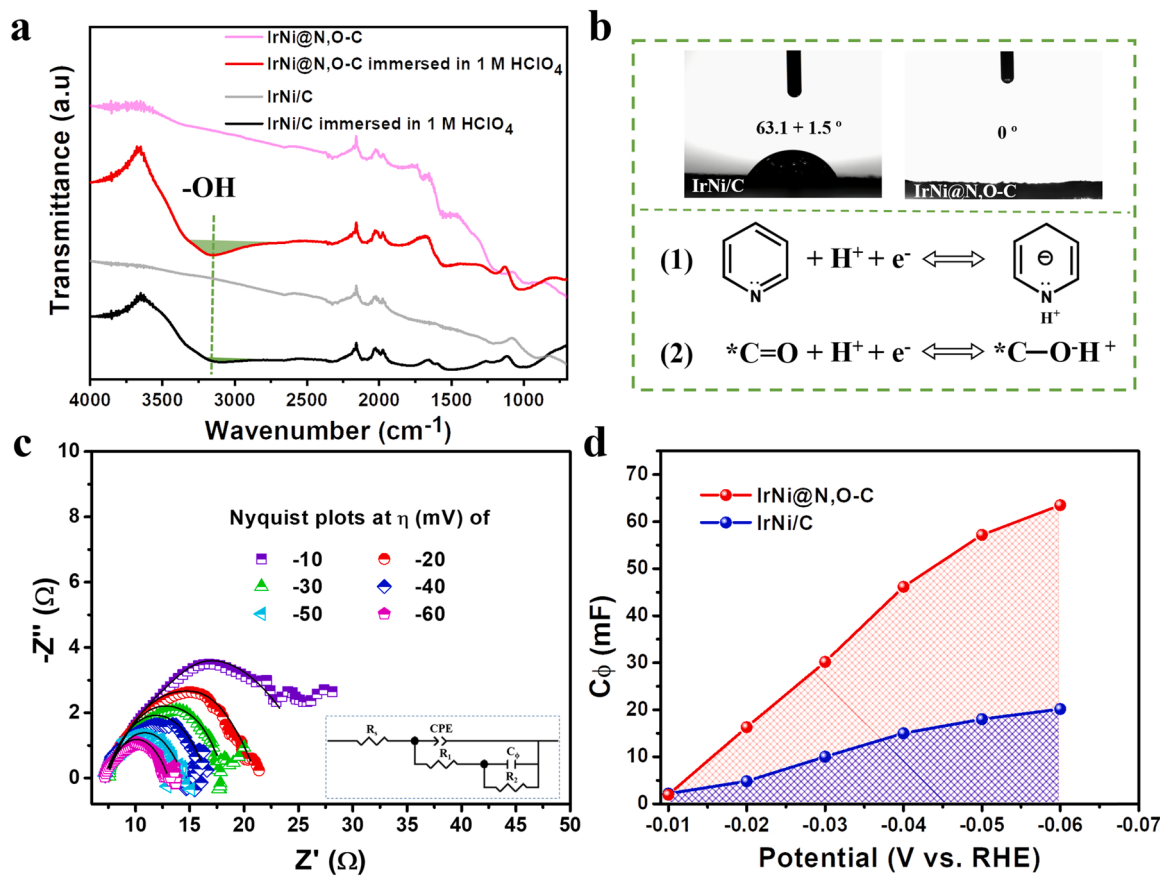


**Fig. 6.** Experimental investigations of the high HER performance. a, FT-IR spectra of IrNi@N,O-C, IrNi@N,O-C immersed in 1 M  $\text{HClO}_4$ , IrNi/C, and IrNi/C immersed in 1 M  $\text{HClO}_4$ . b, Top: water contact angles of IrNi@N,O-C and IrNi/C. Bottom: typical faradaic pseudo-capacitance redox reaction upon N and O functional groups. c, Nyquist plots of IrNi@N,O-C at different overpotentials. Inset: the fitting circuit. d, The calculated  $C_\phi$  of IrNi@N,O-C at different potentials.

has been investigated through the *in situ* EIS measurements at different overpotentials. The obtained Nyquist plots are fitted by a double-parallel equivalent circuit model [49,71,72] (Fig. 6c and Fig. S31, Supporting Information) and the results are displayed in Table S4 (Supporting Information). Herein, the  $R_s$  refers to the uncompensated solution resistance and the CPE and  $R_1$  relate to the charge-transfer kinetics [71]. The  $R_2$  and  $C_\phi$  reflect the  $\text{H}^*$  adsorption resistance and the corresponding pseudo-capacitance, which can depict the  $\text{H}^*$  adsorption behavior over catalyst surface [72]. The  $R_2$  decreases with the increasing overpotential for both IrNi@N,O-C and IrNi/C while the  $R_2$  of IrNi@N,O-C is much smaller than that of IrNi/C at every same overpotential, indicating the more favorable  $\text{H}^*$  adsorption over IrNi@N,O-C. The adsorption pseudo-capacitance  $C_\phi$  giving the  $\text{H}^*$  adsorption charge could be used to describe the  $\text{H}^*$  coverage over catalyst surface. As shown in Fig. 6d, the IrNi@N,O-C shows much higher  $C_\phi$  at every same potential and greater increment trend relative to IrNi/C, suggesting the higher  $\text{H}^*$  coverage for IrNi@N,O-C. For instance, the  $C_\phi$  of IrNi@N,O-C at overpotential of 50 mV is 57.1 mF, which is 3.17 times higher than that of IrNi/C (18.0 mF). Considering the relatively weak absorption of  $\text{H}^*$  on Ir-based catalysts [17,73,74], the great enhancement of  $\text{H}^*$  absorption will largely accelerate the related HER kinetics.

According to above results, the N and O dopants in IrNi@N,O-C nanoreactor may play the proton-adsorbing role on raising  $\text{H}^*$  coverage at the perimeter of IrNi active centers, resulting in the accelerated reaction kinetics and thus enhanced HER performances. It is worth noting that the organic ligands in the near coordination position to the metal centers function as proton relays towards promoted  $\text{H}_2$  generation for hydrogenases [44–46]. In this case of nanoreactor structure, the N,O-C nanocages rich in proton-adsorbing N/O sites, similar to the proton relay function of organic ligands in hydrogenase,

can supply the adequate and available  $\text{H}^+$  to the confined IrNi active centers for the following  $\text{H}_2$  generation. For HER at high current density region, the  $\text{H}^+$  is consumed fast. Therefore, the expedient and rapid supply of  $\text{H}^+$  will improve greatly the reaction kinetics and lower the overpotential, evidenced by the catalytic performances. To further confirm positive effect of N/O dopants on HER performance, the IrNi@N,O-C has been subjected to  $\text{H}_2$  reduction treatment and then the obtained IrNi@N,O-C- $\text{H}_2$  with decreased N/O contents shows declining HER kinetics and activity as compared to the initial IrNi@N,O-C (Fig. S32, Supporting Information), verifying the substantial contribution of N/O dopants on HER performances.

Density functional theory (DFT) calculations have also been performed to gain more insights about the outstanding HER performance of IrNi@N,O-C. Firstly, the optimized structures of graphene, IrNi cluster anchored on graphene (IrNi/C), and IrNi cluster anchored on the N/O co-doped graphene (IrNi@N,O<sub>1/2</sub>-C) are obtained, respectively (Fig. 7a and Fig. S33, Supporting Information). It should be noted that different IrNi@N,O<sub>1/2</sub>-C models are considered, in which IrNi@N,O<sub>1</sub>-C refers to the N/O co-doping in the form of the pyridinic-N and O-C-O groups while IrNi@N,O<sub>2</sub>-C represents the case of the pyridinic-N and \*C=O groups. Then the optimized structures for hydrogen adsorption on IrNi/C and IrNi@N,O<sub>1/2</sub>-C are calculated (Fig. 7b). The obtained HER process with typical three-state diagram [48,49] including an initial  $\text{H}^+$ , an intermediate  $\text{H}^*$  and final  $\text{H}_2$  product is depicted in Fig. 7c. The first step involves  $\text{H}^*$  adsorption on graphitic carbon sites (site-a) with a very high free energy (1.3 eV) for IrNi/C, indicative of an unfavorable adsorption step. In sharp contrast, with introduction of N and O dopants (IrNi@N,O<sub>1</sub>-C) the free energy of the first step on site-a decreases to 0.34 eV, suggesting enhanced  $\text{H}^*$  adsorption. Further, upon \*C=O groups the adsorption of  $\text{H}^*$  is  $-0.42$  eV, indicating the first step on IrNi@N,O<sub>2</sub>-C

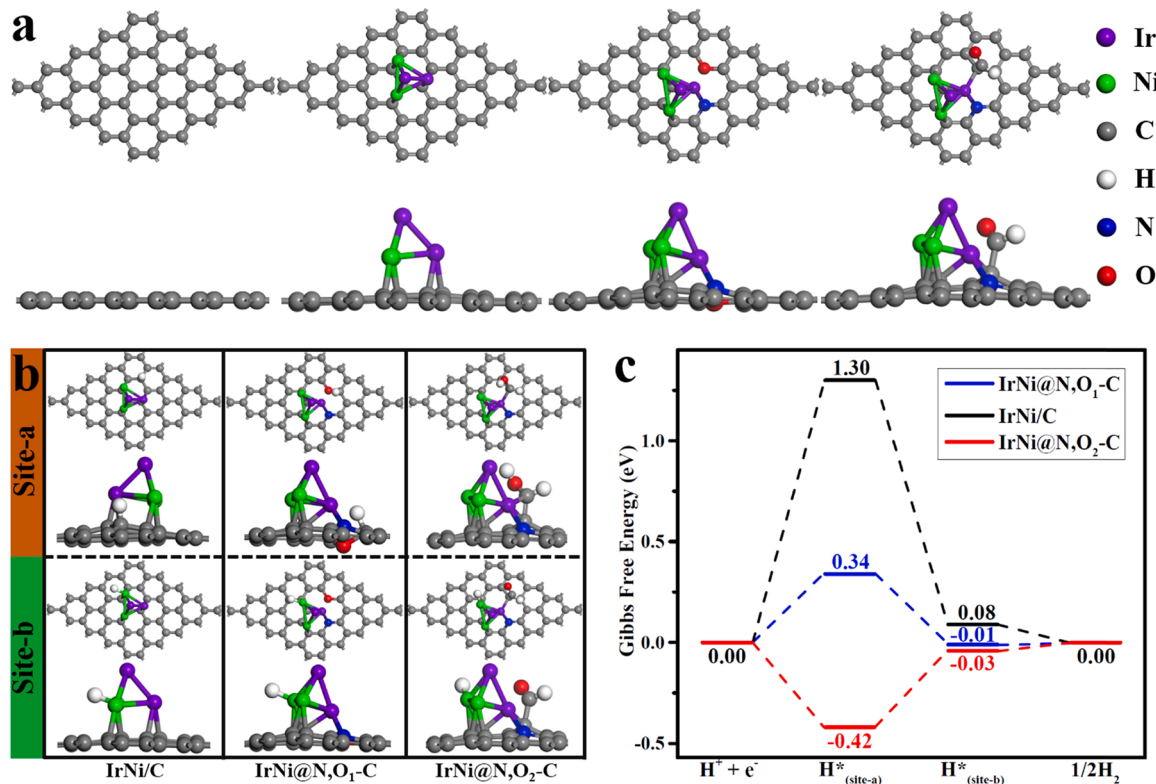


**Fig. 7.** DFT simulations of HER. a, Top and side views of the optimized structure of graphene, IrNi/C and IrNi@N,O<sub>1/2</sub>-C. b, Hydrogen adsorption configurations for IrNi/C and IrNi@N,O<sub>1/2</sub>-C. c, Free energy diagrams of HER for IrNi/C and IrNi@N,O<sub>1/2</sub>-C.

is thermodynamically favorable. The above discussion is consistent with the experimental results and the recently reported results [75] that the \*C=O groups can promote H\* adsorption.

Generally,  $\Delta G_{H^*}$  is regarded as the descriptor to evaluate the HER catalytic activity of different catalysts [76]. An ideal HER catalyst is expected to show an optimal  $\Delta G_{H^*}$  value being close to zero, favoring for the H\* adsorption and subsequent H<sub>2</sub> production. On the IrNi/C surface, the H\* exhibits weak adsorption over IrNi cluster (Fig. 7b) with  $\Delta G_{H^*}$  being 0.08 eV (site-b, Fig. 7c). The slightly positive value of  $\Delta G_{H^*}$  suggests that the IrNi cluster is favorable for H<sub>2</sub> generation but possesses relatively insufficient ability for H\* adsorption. By introducing N and O dopants on graphene, the H\* adsorption on site-b decreases to -0.01 eV for IrNi@N,O<sub>1</sub>-C and -0.03 eV for IrNi@N,O<sub>2</sub>-C, indicating an enhanced H\* adsorption and favorable reaction kinetics. Considering the entire HER pathway, IrNi@N,O<sub>2</sub>-C with favorable H\* adsorption and small  $\Delta G_{H^*}$  may be superior to that of IrNi@N,O<sub>1</sub>-C and accord better with the experiment results. Besides, the transferred H\* adsorption pathway will leave more space on IrNi sites for fast H<sub>2</sub> generation. Additionally, the absolute value of  $\Delta G_{H^*}$  on IrNi@N,O<sub>2</sub>-C is much smaller than that of the Pt (111) surface (Fig. S34, Supporting Information), i.e. |-0.03| for IrNi@N,O<sub>2</sub>-C vs |-0.09| for Pt (111), indicating the superior HER catalytic activity for IrNi@N,O-C.

Furthermore, we also compare the N/O co-doped systems to single doped systems. The single O and N doped materials (IrNi@O-C and IrNi@N-C) with structure similar to IrNi@N,O-C have been prepared (Fig. S35 and S36, Supporting Information). As shown in Fig. S37 (Supporting Information), IrNi@O-C and IrNi@N-C present inferior HER performances to IrNi@N,O-C, in accordance with the DFT calculation results (Fig. S38, Supporting Information). Additionally, using this proposed reactive template strategy, the PtNi@N,O-C and RuNi@N,O-C could be synthesized and they also show impressive HER performances (Fig. S39, Supporting Information). According to above experimental and theoretical results, the N,O-C nanocage-mediated HER pathway contributes to the enhanced HER performances, which is similar to the

hydrogen evolution behavior for hydrogenase enzyme. To the best of our knowledge, there are essential differences between our designed IrNi@N,O-C and the previously reported IrNi alloy catalysts, such as the nanostructure, HER mechanism, and HER performances (Table S5, Supporting Information). Distinguishing from the previously reported IrNi alloy catalysts, the present work focuses on the unique nanoreactor nanostructure with the individual IrNi nanoparticle separately confined in N/O co-doped carbon nanocage, the N,O-C nanocage-mediated HER pathway and outstanding HER performances with high mass activity, rapid reaction kinetics and stability.

#### 4. Conclusion

In this work, inspired by the hydrogen evolution behavior on hydrogenase enzyme, we propose a new strategy to enhance HER activity and stability through coupling inorganic solid proton-adsorbing sites around the metal active sites in a nanoreactor catalyst. The designed IrNi@N,O-C nanoreactor catalyst, with the individual IrNi nanoparticle separately confined in N/O co-doped carbon nanocage, exhibits outstanding HER performances with ultrahigh mass activity, fast reaction kinetics and remarkable stability. A series of experiments demonstrate the N and O dopants in IrNi@N,O-C can readily adsorb the proton and then increase the H\* coverage over IrNi active centers, resulting in the much enhanced HER kinetics. Theoretical studies further unveil that with the assistance of N and O dopants, there is an optimized HER reaction pathway occurring on IrNi@N,O-C with low reaction barriers. This work not only presents a fresh route to synthesize a unique nanoreactor catalyst for efficient catalysis of HER, but also affords new insights and design strategies for the targeted development of high-performance electrocatalysts towards diverse electrocatalytic reactions.

#### CRediT authorship contribution statement

Shanyong Chen: Conceptualization, Methodology, Software,

Formal analysis, Writing – original draft, Visualization. **Shiyan Wang**: Software, Data curation, Writing – review & editing. **Panpan Hao**: Validation, Investigation. **Muhong Li**: Software, Visualization. **Yu Zhang**: Validation, Resources. **Jia Guo**: Resources, Data Curation. **Weiping Ding**: Formal analysis, Project administration. **Min Liu**: Supervision. **Jinlan Wang**: Supervision, Writing – review & editing. **Xuefeng Guo**: Supervision, Writing – review & editing, Funding acquisition.

### Declaration of Competing Interest

The authors declare that they have no known competing financial interests or personal relationships that could have appeared to influence the work reported in this paper.

### Acknowledgement

This work was financially supported by the National Science Foundation of China (22172073, 21773112, 21173119, and 21273109), the National Key Technology Research and Development Program of China (2017YFB0310704), the Opening Project of Key Laboratory of Optoelectronic Chemical Materials and Devices, Ministry of Education, Jianghan University (JDGD-201702), Fundamental Research Funds for the Central Universities and the Hubei Key Laboratory for Processing and Application of Catalytic Materials (CH201401). The authors thank the Hefei Synchrotron Radiation Facility (MCD, NSRL) for helps in characterizations.

### Authors' contribution

S.Y.C implemented material preparation, electrochemical test and manuscript writing. S.Y.W performed the theoretical calculations and data analysis. P.P.H. and M.H.L. took part in XRD and TEM characterization. Y.Z. and J.G. participated in electrochemical test and manuscript writing. W.P.D. provided helpful suggestions for the data analysis. X.F.G., J.L.W., and M. L. supervised this work and guided this study.

### Appendix A. Supporting information

Supplementary data associated with this article can be found in the online version at [doi:10.1016/j.apcatb.2021.120996](https://doi.org/10.1016/j.apcatb.2021.120996).

### References

- [1] C.-T. Dinh, A. Jain, F.P.G. de Arquer, P. De Luna, J. Li, N. Wang, X. Zheng, J. Cai, B. Z. Gregory, O. Voznyy, B. Zhang, M. Liu, D. Sinton, E.J. Crumlin, E.H. Sargent, Multi-site electrocatalysts for hydrogen evolution in neutral media by destabilization of water molecules, *Nat. Energy* 4 (2019) 107–114.
- [2] Q. Chen, B. Wei, Y. Wei, P. Zhai, W. Liu, X. Gu, Z. Yang, J. Zuo, R. Zhang, Y. Gong, Synergistic effect in ultrafine PtNiP nanowires for highly efficient electrochemical hydrogen evolution in alkaline electrolyte, *Appl. Catal. B Environ.* 301 (2022), 120754.
- [3] C. Tang, H.-F. Wang, Q. Zhang, Multiscale principles to boost reactivity in gas-involving energy electrocatalysis, *Acc. Chem. Res.* 51 (2018) 881–889.
- [4] Y. Wen, J. Qi, D. Zhao, J. Liu, P. Wei, X. Kang, X. Li, O doping hierarchical NiCoP/Ni2P hybrid with modulated electron density for efficient alkaline hydrogen evolution reaction, *Appl. Catal. B Environ.* 293 (2021), 120196.
- [5] Z.W. Seh, J. Kibsgaard, C.F. Dickens, I. Chorkendorff, J.K. Nørskov, T.F. Jaramillo, Combining theory and experiment in electrocatalysis: Insights into materials design, *Science* 355 (2017) eaad4998.
- [6] B. Zhu, R. Zou, Q. Xu, Metal-organic framework based catalysts for hydrogen evolution, *Adv. Energy Mater.* 8 (2018), 1801193.
- [7] J. Chen, M. Qin, S. Ma, R. Fan, X. Zheng, S. Mao, C. Chen, Y. Wang, Rational construction of Pt/PtTex interface with optimal intermediate adsorption energy for efficient hydrogen evolution reaction, *Appl. Catal. B Environ.* 299 (2021), 120640.
- [8] C. Zhu, Q. Xian, Q. He, C. Chen, W. Zou, C. Sun, S. Wang, X. Duan, Edge-rich bicrystalline 1T/2H-MoS<sub>2</sub> cocatalyst-decorated {110} terminated CeO<sub>2</sub> nanorods for photocatalytic hydrogen evolution, *ACS Appl. Mater. Interfaces* 13 (2021) 35818–35827.
- [9] D. Voiry, H. Yamaguchi, J. Li, R. Silva, D.C.B. Alves, T. Fujita, M. Chen, T. Asefa, V. B. Shenoy, G. Eda, M. Chhowalla, Enhanced catalytic activity in strained chemically exfoliated WS<sub>2</sub> nanosheets for hydrogen evolution, *Nat. Mater.* 12 (2013) 850–855.
- [10] J.K. Nørskov, C.H. Christensen, Toward efficient hydrogen production at surfaces, *Science* 312 (2006) 1322.
- [11] T. Chen, J. Ma, S. Chen, Y. Wei, C. Deng, J. Chen, J. Hu, W. Ding, Construction of heterostructured CoP/CN/Ni: Electron redistribution towards effective hydrogen generation and oxygen reduction, *Chem. Eng. J.* 415 (2021), 129031.
- [12] R. Subbaraman, D. Tripkovic, D. Strmenik, K.-C. Chang, M. Uchimura, A. P. Paulikas, V. Stamenovic, N.M. Markovic, Enhancing hydrogen evolution activity in water splitting by tailoring Li<sup>+</sup>-Ni(OH)<sub>2</sub>-Pt interfaces, *Science* 334 (2011) 1256–1260.
- [13] H. Zhang, P. An, W. Zhou, B.Y. Guan, P. Zhang, J. Dong, X.W. Lou, Dynamic traction of lattice-confined platinum atoms into mesoporous carbon matrix for hydrogen evolution reaction, *Sci. Adv.* 4 (2018) eaao6657.
- [14] N. Cheng, S. Stambula, D. Wang, M.N. Banis, J. Liu, A. Riese, B. Xiao, R. Li, T.-K. Sham, L.-M. Liu, G.A. Botton, X. Sun, Platinum single-atom and cluster catalysis of the hydrogen evolution reaction, *Nat. Commun.* 7 (2016) 13638.
- [15] C. Xie, W. Chen, S. Du, D. Yan, Y. Zhang, J. Chen, B. Liu, S. Wang, In-situ phase transition of WO<sub>3</sub> boosting electron and hydrogen transfer for enhancing hydrogen evolution on Pt, *Nano Energy* 71 (2020), 104653.
- [16] C. Guo, Y. Jiao, Y. Zheng, J. Luo, K. Davey, S.-Z. Qiao, Intermediate modulation on noble metal hybridized to 2D metal-organic framework for accelerated water electrocatalysis, *Chem* 5 (2019) 2429–2441.
- [17] F. Li, G.-F. Han, H.-J. Noh, J.-P. Jeon, I. Ahmad, S. Chen, C. Yang, Y. Bu, Z. Fu, Y. Liu, J.-B. Baek, Balancing hydrogen adsorption/desorption by orbital modulation for efficient hydrogen evolution catalysis, *Nat. Commun.* 10 (2019) 060.
- [18] Y. Pi, Q. Shao, P. Wang, J. Guo, X. Huang, General formation of monodisperse IrM (M = Ni, Co, Fe) bimetallic nanoclusters as bifunctional electrocatalysts for acidic overall water splitting, *Adv. Funct. Mater.* 27 (2017), 1700886.
- [19] M. Sheng, B. Jiang, B. Wu, F. Liao, X. Fan, H. Lin, Y. Li, Y. Lifshitz, S.-T. Lee, M. Shao, Approaching the volcano top: iridium/silicon nanocomposites as efficient electrocatalysts for the hydrogen evolution reaction, *ACS Nano* 13 (2019) 2786–2794.
- [20] P. Jiang, H. Huang, J. Diao, S. Gong, S. Chen, J. Lu, C. Wang, Z. Sun, G. Xia, K. Yang, Y. Yang, L. Wei, Q. Chen, Improving electrocatalytic activity of iridium for hydrogen evolution at high current densities above 1000 mA cm<sup>-2</sup>, *Appl. Catal. B Environ.* 258 (2019), 117965.
- [21] J. Mahmood, M.A.R. Anjum, S.-H. Shin, I. Ahmad, H.-J. Noh, S.-J. Kim, H.Y. Jeong, J.S. Lee, J.-B. Baek, Encapsulating iridium nanoparticles inside a 3D Cage-like organic network as an efficient and durable catalyst for the hydrogen evolution reaction, *Adv. Mater.* 30 (2018), 1805606.
- [22] J.K. Nørskov, T. Bligaard, A. Logadottir, J.R. Kitchin, J.G. Chen, S. Pandelov, U. Stimming, Trends in the exchange current for hydrogen evolution, *J. Electrochem. Soc.* 152 (2005) J23.
- [23] S. Ye, F. Luo, Q. Zhang, P. Zhang, T. Xu, Q. Wang, D. He, L. Guo, Y. Zhang, C. He, X. Ouyang, M. Gu, J. Liu, X. Sun, Highly stable single Pt atomic sites anchored on aniline-stacked graphene for hydrogen evolution reaction, *Energy Environ. Sci.* 12 (2019) 1000–1007.
- [24] H. Li, K. Liu, J. Fu, K. Chen, K. Yang, Y. Lin, B. Yang, Q. Wang, H. Pan, Z. Cai, H. Li, M. Cao, J. Hu, Y.-R. Lu, T.-S. Chan, E. Cortés, A. Fratalocchi, M. Liu, Paired Ru-O-Mo ensemble for efficient and stable alkaline hydrogen evolution reaction, *Nano Energy* 82 (2021), 105767.
- [25] K. Xiang, D. Wu, X. Deng, M. Li, S. Chen, P. Hao, X. Guo, J.-L. Luo, X.-Z. Fu, Boosting H<sub>2</sub> generation coupled with selective oxidation of methanol into value-added chemical over cobalt hydroxide@hydroxysulfide nanosheets electrocatalysts, *Adv. Funct. Mater.* 30 (2020), 1909610.
- [26] Y. Pi, Q. Shao, X. Zhu, X. Huang, Dynamic structure evolution of composition segregated iridium-nickel rhombic dodecahedra toward efficient oxygen evolution electrocatalysis, *ACS Nano* 12 (2018) 7371–7379.
- [27] Y. Wang, L. Zhang, K. Yin, J. Zhang, H. Gao, N. Liu, Z. Peng, Z. Zhang, Nanoporous iridium-based alloy nanowires as highly efficient electrocatalysts toward acidic oxygen evolution reaction, *ACS Appl. Mater. Interfaces* 11 (2019) 39728–39736.
- [28] N. Liu, K. Yin, C. Si, T. Kou, Y. Zhang, W. Ma, Z. Zhang, Hierarchically porous nickel-iridium-ruthenium-aluminum alloys with tunable compositions and electrocatalytic activities towards the oxygen/hydrogen evolution reaction in acid electrolyte, *J. Mater. Chem. A* 8 (2020) 6245–6255.
- [29] M.-T. Chen, R.-L. Zhang, J.-J. Feng, L.-P. Mei, Y. Jiao, L. Zhang, A.-J. Wang, A facile one-pot room-temperature growth of self-supported ultrathin rhodium-iridium nanosheets as high-efficiency electrocatalysts for hydrogen evolution reaction, *J. Colloid Interf. Sci.* 606 (2022) 1707–1714.
- [30] M.-T. Chen, J.-J. Duan, J.-J. Feng, L.-P. Mei, Y. Jiao, L. Zhang, A.-J. Wang, Iron, rhodium-codoped Ni2P nanosheets arrays supported on nickel foam as an efficient bifunctional electrocatalyst for overall water splitting, *J. Colloid Interf. Sci.* 605 (2022) 888–896.
- [31] M. Li, K. Duanmu, C. Wan, T. Cheng, L. Zhang, S. Dai, W. Chen, Z. Zhao, P. Li, H. Fei, Y. Zhu, R. Yu, J. Luo, K. Zang, Z. Lin, M. Ding, J. Huang, H. Sun, J. Guo, X. Pan, W.A. Goddard III, P. Sautet, Y. Huang, X. Duan, Single-atom tailoring of platinum nanocatalysts for high-performance multifunctional electrocatalysis, *Nat. Catal.* 2 (2019) 495–503.
- [32] K. Li, Y. Li, Y. Wang, J. Ge, C. Liu, W. Xing, Enhanced electrocatalytic performance for the hydrogen evolution reaction through surface enrichment of platinum nanoclusters alloying with ruthenium in situ embedded in carbon, *Energy Environ. Sci.* 11 (2018) 1232–1239.
- [33] X. Wang, Y. Zhu, A. Vasileff, Y. Jiao, S. Chen, L. Song, B. Zheng, Y. Zheng, S.-Z. Qiao, Strain effect in bimetallic electrocatalysts in the hydrogen evolution reaction, *ACS Energy Lett.* 3 (2018) 1198–1204.

[34] Z. Li, J.-Y. Fu, Y. Feng, C.-K. Dong, H. Liu, X.-W. Du, A silver catalyst activated by stacking faults for the hydrogen evolution reaction, *Nat. Catal.* 2 (2019) 1107–1114.

[35] X.-P. Yin, H.-J. Wang, S.-F. Tang, X.-L. Lu, M. Shu, R. Si, T.-B. Lu, Engineering the coordination environment of single-atom platinum anchored on graphdiyne for optimizing electrocatalytic hydrogen evolution, *Angew. Chem. Int. Ed.* 57 (2018) 9382–9386.

[36] B. Lu, L. Guo, F. Wu, Y. Peng, J.E. Lu, T.J. Smart, N. Wang, Y.Z. Finfrock, D. Morris, P. Zhang, N. Li, P. Gao, Y. Ping, S. Chen, Ruthenium atomically dispersed in carbon outperforms platinum toward hydrogen evolution in alkaline media, *Nat. Commun.* 10 (2019) 631.

[37] L. Zhang, Y. Jia, H. Liu, L. Zhuang, X. Yan, C. Lang, X. Wang, D. Yang, K. Huang, S. Feng, X. Yao, Charge polarization from atomic metals on adjacent graphitic layers for enhancing the hydrogen evolution reaction, *Angew. Chem. Int. Ed.* 58 (2019) 9404–9408.

[38] S. Chen, C. Lv, L. Liu, M. Li, J. Liu, J. Ma, P. Hao, X. Wang, W. Ding, M. Xie, X. Guo, High-temperature treatment to engineer the single-atom Pt coordination environment towards highly efficient hydrogen evolution, *J. Energy Chem.* 59 (2021) 212–219.

[39] Z. Luo, H. Zhang, Y. Yang, X. Wang, Y. Li, Z. Jin, Z. Jiang, C. Liu, W. Xing, J. Ge, Reactant friendly hydrogen evolution interface based on di-anionic MoS<sub>2</sub> surface, *Nat. Commun.* 11 (2020) 1116.

[40] D. Strmcnik, M. Uchimura, C. Wang, R. Subbaraman, N. Danilovic, D. van der Vliet, A.P. Paulikas, V.R. Stamenkovic, N.M. Markovic, Improving the hydrogen oxidation reaction rate by promotion of hydroxyl adsorption, *Nat. Chem.* 5 (2013) 300–306.

[41] P.S. Lamoureux, A.R. Singh, K. Chan, pH effects on hydrogen evolution and oxidation over Pt(111): insights from first-principles, *ACS Catal.* 9 (2019) 6194–6201.

[42] I. Ledezma-Yanez, W.D.Z. Wallace, P. Sebastian-Pascual, V. Climent, J.M. Feliu, M. T.M. Koper, Interfacial water reorganization as a pH-dependent descriptor of the hydrogen evolution rate on platinum electrodes, *Nat. Energy* 2 (2017) 17031.

[43] P. Trogadas, M.-O. Cappens, Nature-inspired electrocatalysts and devices for energy conversion, *Chem. Soc. Rev.* 49 (2020) 3107–3141.

[44] D.W. Mulder, Y. Guo, M.W. Ratzloff, P.W. King, Identification of a catalytic iron-hydride at the H-cluster of [FeFe]-hydrogenase, *J. Am. Chem. Soc.* 139 (2017) 83–86.

[45] V. Pelmenschikov, J.A. Birrell, C.C. Pham, N. Mishra, H. Wang, C. Sommer, E. Reijerse, C.P. Richers, K. Tamasaku, Y. Yoda, T.B. Rauchfuss, W. Lubitz, S. P. Cramer, Reaction coordinate leading to H<sub>2</sub> production in [FeFe]-hydrogenase identified by nuclear resonance vibrational spectroscopy and density functional theory, *J. Am. Chem. Soc.* 139 (2017) 16894–16902.

[46] M.L. Helm, M.P. Stewart, R.M. Bullock, M.R. DuBois, D.L. DuBois, A synthetic nickel electrocatalyst with a turnover frequency above 100,000 s<sup>-1</sup> for H<sub>2</sub> production, *Science* 333 (2011) 863.

[47] P. Rodriguez-Maciá, A. Dutta, W. Lubitz, W.J. Shaw, O. Rüdiger, Direct comparison of the performance of a bio-inspired synthetic nickel catalyst and a [NiFe]-hydrogenase, both covalently attached to electrodes, *Angew. Chem. Int. Ed.* 54 (2015) 12303–12307.

[48] S. Qiu, L.M. Azofra, D.R. MacFarlane, C. Sun, Unraveling the role of ligands in the hydrogen evolution mechanism catalyzed by [NiFe] hydrogenases, *ACS Catal.* 6 (2016) 5541–5548.

[49] J. Li, H.-X. Liu, W. Gou, M. Zhang, Z. Xia, S. Zhang, C.-R. Chang, Y. Ma, Y. Qu, Ethylene-glycol ligand environment facilitates highly efficient hydrogen evolution of Pt/CoP through proton concentration and hydrogen spillover, *Energy Environ. Sci.* 12 (2019) 2298–2304.

[50] G.-R. Xu, J. Rai, L. Yao, Q. Xue, J.-X. Jiang, J.-H. Zeng, Y. Chen, J.-M. Lee, Polyallylamine-functionalized platinum tripods: enhancement of hydrogen evolution reaction by proton carriers, *ACS Catal.* 7 (2017) 452–458.

[51] Y. Ge, J. Liu, X. Liu, J. Hu, X. Duan, X. Duan, Rapid electrochemical cleaning silver nanowire thin films for high-performance transparent conductors, *J. Am. Chem. Soc.* 141 (2019) 12251–12257.

[52] Y. Zhang, T. Qu, K. Xiang, Y. Shen, S. Chen, M. Xie, X. Guo, In situ formation/ carbonization of quinone-amine polymers towards hierarchical porous carbon foam with high faradaic activity for energy storage, *J. Mater. Chem. A* 6 (2018) 2353–2359.

[53] J.P. Perdew, K. Burke, M. Ernzerhof, Generalized gradient approximation made simple, *Phys. Rev. Lett.* 77 (1996) 3865–3868.

[54] P.E. Blöchl, Projector augmented-wave method, *Phys. Rev. B* 50 (1994) 17953–17979.

[55] L.A. Burns, Á.V. Mayagoitia, B.G. Sumpter, C.D. Sherrill, Density-functional approaches to noncovalent interactions: a comparison of dispersion corrections (DFT-D), exchange-hole dipole moment (XDM) theory, and specialized functionals, *J. Chem. Phys.* 134 (2011) 084107.

[56] J. Liang, S. Chen, M. Xie, Y. Wang, X. Guo, W. Ding, Expedited fabrication of flower-like hierarchical mesoporous carbon superstructures as supercapacitor electrode materials, *J. Mater. Chem. A* 2 (2014) 16884–16891.

[57] P. Chen, T. Zhou, L. Xing, K. Xu, Y. Tong, H. Xie, L. Zhang, W. Yan, W. Chu, C. Wu, Y. Xie, Atomically dispersed iron-nitrogen species as electrocatalysts for bifunctional oxygen evolution and reduction reactions, *Angew. Chem. Int. Ed.* 56 (2017) 610–614.

[58] W. Fan, Z. Li, C. You, X. Zong, X. Tian, S. Miao, T. Shu, C. Li, S. Liao, Binary Fe, Cu-doped bamboo-like carbon nanotubes as efficient catalyst for the oxygen reduction reaction, *Nano Energy* 37 (2017) 187–194.

[59] L. Zhou, H. Cao, S. Zhu, L. Hou, C. Yuan, Hierarchical micro-/mesoporous N- and O-enriched carbon derived from disposable cashmere: a competitive cost-effective material for high-performance electrochemical capacitors, *Green. Chem.* 17 (2015) 2373–2382.

[60] H. Zhao, J. Ye, W. Song, D. Zhao, M. Kang, H. Shen, Z. Li, Insights into the surface oxygen functional group-driven fast and stable sodium adsorption on carbon, *ACS Appl. Mater. Interfaces* 12 (2020) 6991–7000.

[61] S. Chen, T. Luo, K. Chen, Y. Lin, J. Fu, K. Liu, C. Cai, Q. Wang, H. Li, X. Li, J. Hu, H. Li, M. Zhu, M. Liu, Chemical identification of catalytically active sites on oxygen-doped carbon nanosheet to decipher the high activity for electro-synthesis hydrogen peroxide, *Angew. Chem. Int. Ed.* 60 (2021) 16607–16614.

[62] S. Guo, S. Zhang, L. Wu, S. Sun, Co/CoO nanoparticles assembled on graphene for electrochemical reduction of oxygen, *Angew. Chem. Int. Ed.* 51 (2012) 11770–11773.

[63] I.C. Gerber, P. Serp, A theory/experience description of support effects in carbon-supported catalysts, *Chem. Rev.* 120 (2020) 1250–1349.

[64] X. Li, W. Liu, M. Zhang, Y. Zhong, Z. Weng, Y. Mi, Y. Zhou, M. Li, J.J. Cha, Z. Tang, H. Jiang, X. Li, H. Wang, Strong metal–phosphide interactions in core–shell geometry for enhanced electrocatalysis, *Nano Lett.* 17 (2017) 2057–2063.

[65] J. Wang, Z. Wei, S. Mao, H. Li, Y. Wang, Highly uniform Ru nanoparticles over N-doped carbon: pH and temperature-universal hydrogen release from water reduction, *Energy Environ. Sci.* 11 (2018) 800–806.

[66] R. Borup, J. Meyers, B. Pivovar, Y.S. Kim, R. Mukundan, N. Garland, D. Myers, M. Wilson, F. Garzon, D. Wood, P. Zelenay, K. More, K. Stroh, T. Zawodzinski, J. Boncella, J.E. McGrath, M. Inaba, K. Miyatake, M. Hori, K. Ota, Z. Ogumi, S. Miyata, A. Nishikata, Z. Siroma, Y. Uchimoto, K. Yasuda, K.-i Kimijima, N. Iwashita, Scientific aspects of polymer electrolyte fuel cell durability and degradation, *Chem. Rev.* 107 (2007) 3904–3951.

[67] Y. Yao, W. Chen, Y. Du, Z. Tao, Y. Zhu, Y.-X. Chen, An electrochemical in situ infrared spectroscopic study of graphene/electrolyte interface under attenuated total reflection configuration, *J. Phys. Chem. C* 119 (2015) 22452–22459.

[68] H. Liu, H. Song, X. Chen, S. Zhang, J. Zhou, Z. Ma, Effects of nitrogen- and oxygen-containing functional groups of activated carbon nanotubes on the electrochemical performance in supercapacitors, *J. Power Sources* 285 (2015) 303–309.

[69] C.-M. Chen, Q. Zhang, X.-C. Zhao, B. Zhang, Q.-Q. Kong, M.-G. Yang, Q.-H. Yang, M.-Z. Wang, Y.-G. Yang, R. Schloegl, D.S. Su, Hierarchically gminated graphene honeycomb for electrochemical capacitive energy storage, *J. Mater. Chem.* 22 (2012) 14076–14084.

[70] J. Wordsworth, T.M. Benedetti, A. Alinezhad, R.D. Tilley, M.A. Edwards, W. Schuhmann, J.J. Gooding, The importance of nanoscale confinement to electrocatalytic performance, *Chem. Sci.* 11 (2020) 1233–1240.

[71] A. Damian, S. Omanovic, Ni and Ni-Mo hydrogen evolution electrocatalysts electrodeposited in a polyaniline matrix, *J. Power Sources* 158 (2006) 464–476.

[72] N.V. Krstajic, B.N. Grgur, N.S. Mladenovic, M.V. Vojnovic, M.M. Jaksic, The determination of kinetics parameters of the hydrogen evolution on Ti-Ni alloys by ac impedance, *Electrochim. Acta* 42 (1997) 323–330.

[73] J.R. Engstrom, W. Tsai, W.H. Weinberg, The chemisorption of hydrogen on the (111) and (110)-(1×2) surfaces of iridium and platinum, *J. Chem. Phys.* 87 (1987) 3104–3119.

[74] E. Skulason, V. Tripkovic, M.E. Bjorketun, S. Gudmundsdottir, G. Karlberg, J. Rossmeisl, T. Bligaard, H. Jonsson, J.K. Norskov, Modeling the electrochemical hydrogen oxidation and evolution reactions on the basis of density functional theory calculations, *J. Phys. Chem. C* 114 (2010) 18182–18197.

[75] Y. Xue, L. Hui, H. Yu, Y. Liu, Y. Fang, B. Huang, Y. Zhao, Z. Li, Y. Li, Rationally engineered active sites for efficient and durable hydrogen generation, *Nat. Commun.* 10 (2019) 2281.

[76] C. Ling, Y. Ouyang, L. Shi, S. Yuan, Q. Chen, J. Wang, Template-grown MoS<sub>2</sub> nanowires catalyze the hydrogen evolution reaction: ultralow kinetic barriers with high active site density, *ACS Catal.* 7 (2017) 5097–5102.